Experimental and Numerical Investigation of the Performance of Vortex Generators on Separation Control

Velte, Clara Marika; Hansen, Martin Otto Laver; Jønck, Kasper Martin

Published in:
Journal of Physics: Conference Series (Online)

Link to article, DOI:
10.1088/1742-6596/75/1/012030

Publication date:
2007

Document Version
Publisher's PDF, also known as Version of record

Journal of Physics: Conference Series **75** (2007) 012030 doi:10.1088/1742-6596/75/1/012030

Experimental and numerical investigation of the performance of vortex generators on separation control

C M Velte, M O L Hansen and K Jønck

Technical University of Denmark, Department of Mechanical Engineering, Fluid Mechanics Section, 2800 Kgs. Lyngby, Denmark

E-mail: cve@mek.dtu.dk

Abstract. An experimental wind tunnel study of the flow past a row of counter-rotating vortex generators mounted on top of a bump has been performed. All three velocity components are measured in spanwise planes downstream of the vortex generators using Stereoscopic Particle Image Velocimetry, SPIV. The objective of this study is to investigate the effect of vortex generators in a separating, low Reynolds number, turbulent boundary layer over a geometry which is generating an adverse pressure gradient. The flow behaves as expected, in the sense that the vortices transport high momentum fluid into the boundary layer, making it thinner and more resistant to the adverse pressure gradient with respect to separation. The idea behind the experiments is that the results will be offered for validation of modeling of the effect of vortex generators using various numerical codes. Steady-state RANS computations have been carried out in parallel to the experiments. The computations are able to capture the overall flow structure, but has difficulties predicting the flow in the separation region and the large scale convection due to the vortex generators.

1. Introduction

For some industrial flows it is beneficial to transfer high momentum fluid from the outer flow into the boundary layer. This principle can e.g. be used to increase the fluid temperature near a wall in a heat exchanger or to increase the momentum in a boundary layer exposed to an adverse pressure gradient in order to delay separation (see e.g. [1]). This mixing can be achieved by various methods, e.g. by enhancement of turbulence using so-called turbulators, or by creating a large scale vortex structure in the streamwise direction that by convection mixes the flow. Taylor introduced so-called Vortex Generators (VGs) in 1947 [2], which basically are small rectangular or triangular plates glued to the surface with an angle of incidence to the main flow, see figure 1.

These plates act as small wings and the tip vortices are convected downstream and mix high momentum or high temperature flow into the boundary layer. One would expect that the height of the vortex generator should be approximately the same as the boundary layer thickness, δ, but Lin [3] has showed that in a highly turbulent boundary layer, they can have a large effect even at a height of approximately 0.2δ due to the large near wall gradient of the streamwise velocity component. This type of vortex generator is denoted submerged, low profile or micro VG and one advantage is that they yield lesser drag penalty. Vortex generators can be positioned to

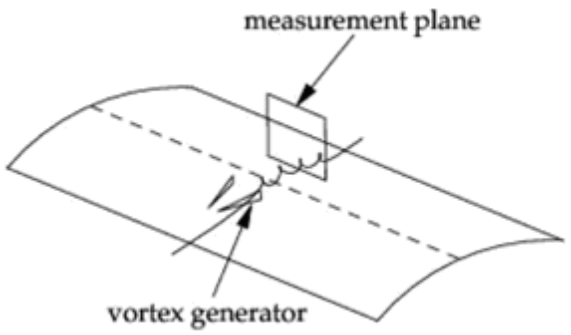

Figure 1. Schematic effect of vortex generators and positioning of measurement plane.

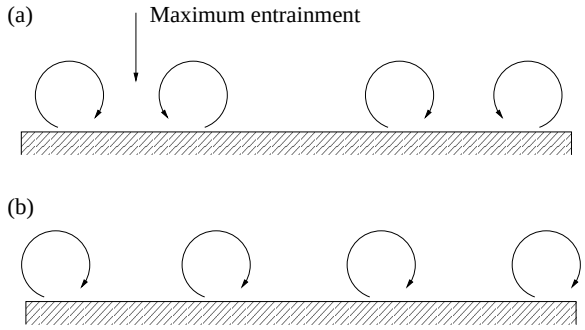

Figure 2. Vortical motion created by pairs of a) counter-rotating and b) co-rotating devices.

Table 1. Optimal geometrical parameters for vortex generators, [4].

h/δ	l/h	L/h	λ/h	β
0.37	2	2.5	6	18°

generate co- or counter-rotating vortices (see figure 2) and it has been shown by Godard and Stanislas [4] that they work most efficiently when generating counter-rotating vortices with the aid of triangular vanes. In [4] various experiments are performed to further estimate an optimum geometry of the vortex generators and to characterize the flow downstream of the devices. The optimal design parameters found in this study are presented in table 1.

Referring to table 1, h is the device height, l is the device length, L is the distance between the trailing edges of two vortex generators within one pair, λ is the distance between two VG pairs and β is the device angle of incidence. This optimum geometry will, of course, depend on the application and is therefore most likely not universal, but has nevertheless also been used in this experiment. The distance between the devices and the separation line showed a weak dependency, and was therefore not considered in this study. Furthermore, three device heights were tested to investigate the effect on the separation in this particular case. Previous studies have investigated the flow structure of longitudinal vortices generated by VGs (see e.g. [5], [6] and [7]). The application of vortex generators on wind turbine blades can in some cases have quite a dramatic influence on the produced power (see [8]) and they are therefore often used on commercial wind turbine blades.

The main purpose in the present work is to create a detailed database of the flow behind vortex generators in a controlled experiment in order to be used for later code validation of efficient and accurate CFD modeling of the effect of vortex generators. The experimental method chosen to characterize the flow is Stereoscopic Particle Image Velocimetry (SPIV). This method enables one to measure the complete, instantaneous velocity field quantitatively throughout the entire measurement plane. Therefore SPIV has the advantage of providing a good basis for code validation as well as enabling analysis of instantaneous snapshots of unsteady flow fields.

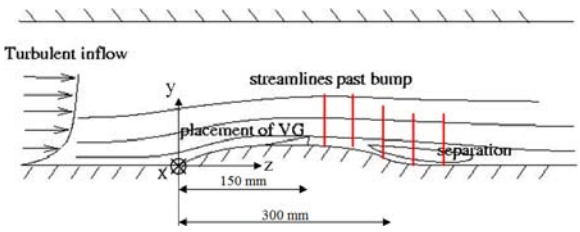

Figure 3. Sketch of the wind tunnel test section, the positioning of measurement planes and definition of coordinate system.

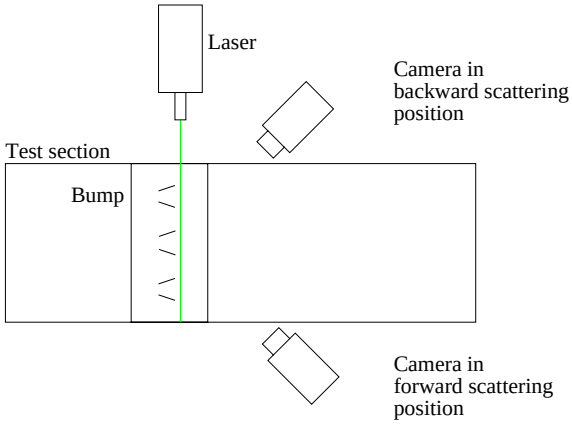

Figure 4. Sketch of the SPIV setup at the test section.

2. Method

2.1. Experimental Setup

The measurements were carried out in a closed-circuit wind tunnel with an 8 : 1 contraction ratio and a test section of cross sectional area 300×600 mm with length 2 m. The suction side of a wind turbine wing is represented by a bump mounted vertically on one of the test section walls with the leading edge positioned 600 mm downstream of the inlet grid. The bump is a circular sector, extended in the spanwise direction creating a cylindrical sector with radius 390 mm. The bump height is 30 mm and the chord length and bump width are 300 mm and 600 mm respectively. This model gives rise to an adverse pressure gradient strong enough to generate separation. The experiments were conducted at a free stream velocity of $W = 1$ m/s, corresponding to $Re = 20\ 000$ based on the bump chord length. The turbulent inflow is assured by a turbulence generating inlet grid with mesh length $M = 39$ mm situated at the beginning of the test section. In [9], the turbulence intensity at the inlet has been estimated to 12 % and the boundary layer thickness at the VG position has been measured to be 25 mm.

2.2. Actuators

Triangular vanes with three different heights were investigated, 0.2δ, 0.4δ and 1δ, where δ represents the boundary layer thickness at the position of the devices. The vortex generators were positioned with their trailing edges at 50% bump chord. The geometry and relative positioning can be found in table 1.

2.3. Velocity Measurements and Acquisition of Data

The measurements were conducted in spanwise planes (see figure 1) at various positions downstream of the vortex generators. A sketch of the wind tunnel test section and the positioning of measurement planes is shown in figure 3, where also the coordinate system is defined. The equipment was mounted on a rigid traverse, traversing in the axial and normal directions. This configuration enables one to calibrate only once and perform measurements accurately at the different streamwise positions using the same calibrated configuration. All measurement planes are parallel to each other and their normal component is parallel to the test section walls. The streamwise positioning of the measurement planes varies for the different device heights upstream of $z = 250$ mm, since these positions are chosen according to the device height at use.

A sketch of the experimental setup is found in figure 4. A laser was placed at the top of the test section, illuminating the vertically mounted bump from the side. Two cameras were placed on the same side of the light sheet, resulting in one camera placed in the forward scattering direction and one in the backward scattering one. The angle of each respective camera to the laser sheet was 45°. The f-numbers were set to between 8 and 16 for the camera in the forward scattering direction and 4 or 5.6 for the camera in the backward scattering direction, depending on the light budget of reflections from the particles and the bump and devices at each individual plane. The stereoscopic PIV equipment included a double cavity Solo 120XT Nd-YAG laser (wavelength 532 nm) capable of delivering light pulses of 120 mJ. The light sheet thickness at the measurement position of 2 mm was created using a combination of a spherical convex and a cylindrical concave lens. The equipment also included two Dantec Dynamics HiSense MkII cameras (1344×1024 pixels) equipped with 60 mm lenses and filters designed to only pass light with wavelengths close to that of the laser light. Both cameras were mounted on Scheimpflug angle adjustable mountings. In order to obtain a smaller measurement area, the cameras were, in some of the tests, equipped with teleconverters. The seeding, consisting of glycerol droplets with a diameter of $2-3$ μm, was added to the flow downstream of the test section. The images were processed using Dantec Flowmanager software version 4.7. Adaptive correlation was applied using refinement with an interrogation area size of 32×32 pixels. Local median validation was used in the immediate vicinity of each interrogation area to remove spurious vectors between each refinement step. The overlap between interrogation areas was 50 %. For each measurement position, a sample size of 500 was taken. The recording of image maps was done with an acquisition rate of 1.0 Hz. In order to provide the cameras with the information for reconstruction of the velocity vectors to three component velocities, a calibration was performed. A calibration target was positioned within the light sheet and traversed through the streamwise direction in steps of 0.5 mm through five different positions which were recorded by the two cameras. The mapping function, providing the transformation from the coordinate system of the respective camera to the coordinate system of the calibration target, was obtained from these recordings using a linear transformation. Reflections from objects other than the glycerine particles were removed by subtracting pictures taken at the corresponding position with no particles present in the flow.

2.4. Numerical modeling

The data is obtained from the steady-state RANS equations using $k-\omega$ SST turbulence model by Menter. The simulations were done in Ansys CFX 10.0. The model matched the full spanwise and normal dimensions of the wind tunnel test section. The vortex generators were modeled using a "thin surface"-technique which implies that they are represented by a 2-dimensional surface, i.e. with no thickness. The use of this approach relaxes the meshing requirements in the vicinity of the vortex generators compared to vortex generators modeled with finite thickness. The solutions were obtained on hybrid, unstructured meshes consisting of tetrahedrons, prisms and pyramids. The prisms were used for the inflated boundaries which were implemented on the upper and lower wall with approximately 25 nodes in the normal direction. The mesh size varied between 3 and 4 million elements. y^+ values were in average below 1 for all simulations. The inlet conditions were based on SPIV measurements from which velocity profiles and turbulence quantities were extracted. The equations were discretized using the High Resolution Scheme, which is a hybrid scheme that blends 1st and 2nd order discretization. A blend factor is calculated to obtain the highest order while retaining a bounded solution. Average values of this blend factor were approximately 0.98, a value of 1 indicating pure 2nd order for all cases. The normalized residuals for each component of momentum and the pressure all converged to at least $1e^{-5}$ RMS. All simulations were done using double precision. For each case a grid independency study was performed. The solution for each case was solved on 3 grids of increasing density.

3. Results and Discussion

3.1. Downstream development of vortices

Figure 5 shows the measured velocities on the right and the streamwise vorticity component on the left for four downstream planes (z_{VG}/h = 1, 2, 4 and 8), for $h/\delta = 1$. z_{VG} has the same direction as the z-component, with its origin at the trailing edges of the devices, i.e. $z_{VG} = 0$ at $z = 150$ mm. The secondary velocities are shown as vectors and the streamwise component (out of plane) is shown using colors. Only every fourth vector is shown. One can clearly see that the vortex generators have a strong visible effect on the boundary layer, which becomes significantly thinner in the downwash region where high momentum fluid is being transferred into the near wall region in between these counter-rotating vortices induced by a vortex generator pair. It is also seen how this effect is reduced when moving downstream. The vorticity plots reveal that the vortex generators give rise to primary vortices which in turn generate shear layers due to the presence of the wall.

3.2. Decay of vorticity

The decay of the generated vortices can clearly be seen in figure 6, showing the streamwise development of the maximum of the streamwise vorticity component. This quantity has been normalized with the maximum value in the most upstream plane for each respective case. All three cases show decaying vorticity with axial distance due to viscous effects, as is also seen in the work by others [7]. The maximum vorticity in the $h = 1\delta$ case decays exponentially and has in figure 6 been compared to the function $1.5e^{-0.2\frac{z}{h}}$.

3.3. Volumetric flow rate

Figure 7 shows the magnitude of the volumetric flow rate in the upstream direction, i.e. the amount of reversed flow. This flow rate has been non-dimensionalized with the total flow rate through each measurement plane. The plot thus shows the streamwise development of the separation for the various cases with different device heights and for the case without vortex generators. One can clearly see that all configurations with vortex generators reduce the maximum amount of reversed volumetric flow rate to less than 10 % as compared to the case without vortex generators. However, they do not eliminate the backflow. The largest backflow in the clean case is found at $z = 300$ mm, which can be explained from the discontinuity in the geometry in the model at the border between the trailing edge of the bump and the test section wall. The unsteady point of separation, located at a streamwise position of approximately 210 mm, is not substantially affected by any of the VG configurations, however it is evident that the reattachment point is significantly affected for all of the VG configurations. The most prominent feature of figure 7 is that the reversed flow rate is larger for the 0.4δ case than for the 1δ and 0.2δ cases. This is surprising, since it is expected that the effect of vortex generator height upon reversed flow rate should be monotonic.

In figure 7 it is seen that the largest difference between the VG cases occurs at approximately $z = 250$ mm. In figure 8 the streamwise velocity component is therefore plotted in the first row as colors directly in this plane whereas the second row shows $(w(x, y) - \overline{w}(y))/\overline{w}(y)$, where $w(x, y)$ and $\overline{w}(y)$ denote the local value of the streamwise velocity component and the spanwise averaged value respectively. It is seen that the velocity varies much more in the plane for the case of 0.4δ than for the two other VG heights, which is causing a different effect on reducing the backflow than for the two other device heights.

Figure 9 shows the measured axial and normal velocity profiles at different streamwise positions in the configurations with and without vortex generators in the symmetry plane ($x = 0$ mm). It is again clearly seen that the transfer of high momentum into the boundary layer from the vortex generators decreases the separation behind the bump at this particular spanwise position.

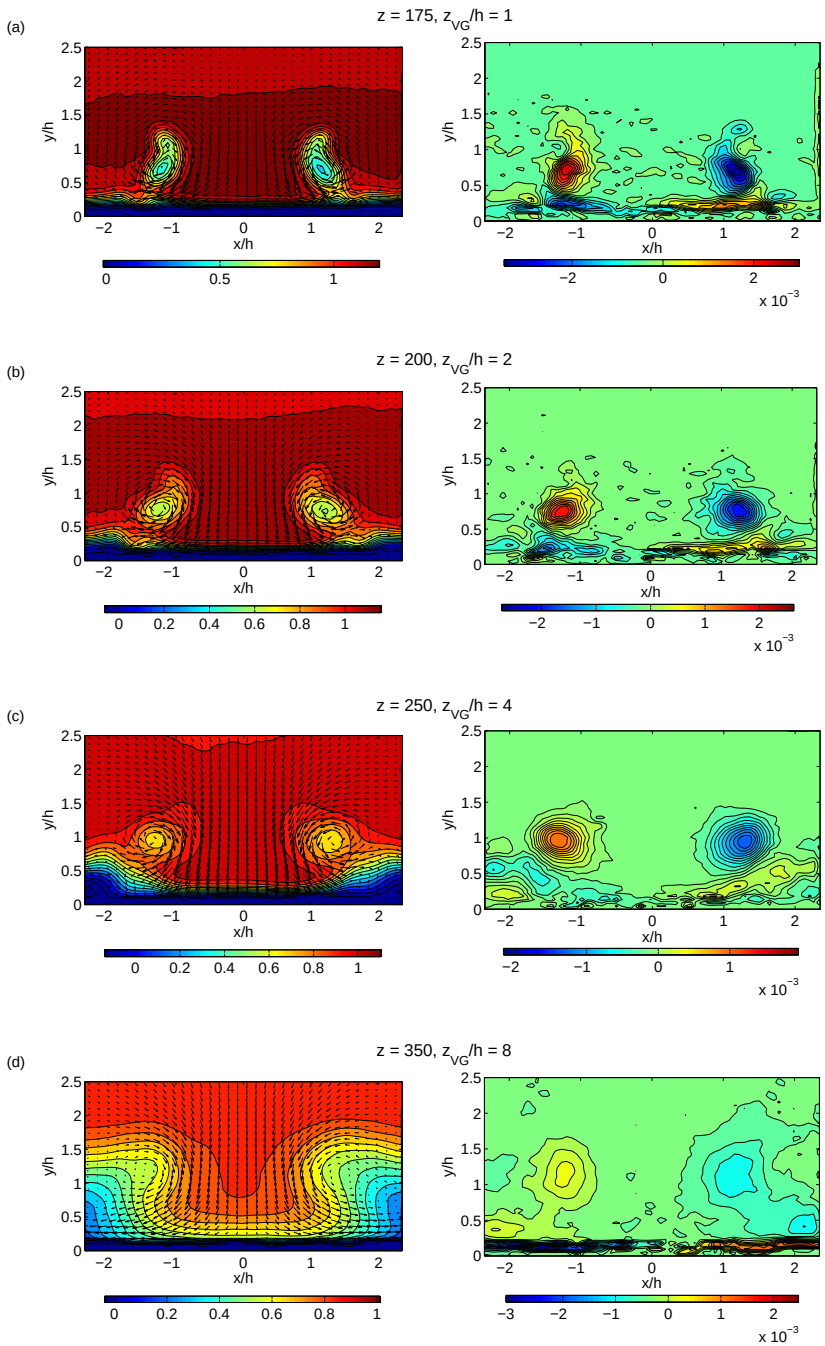

Figure 5. Velocity field plots with in-plane components represented by vectors and the out-of-plane component represented by contours (left column) and corresponding longitudinal vorticity represented by contours (right column) for four positions downstream of vortex generators ((a) $z_{VG}/h = 1$, (b) $z_{VG}/h = 2$, (c) $z_{VG}/h = 4$ and (d) $z_{VG}/h = 8$), $h/\delta = 1$, showing the streamwise development of the flow field. The largest secondary velocities are of the order of 0.5 m/s, which can be compared to the free stream velocity of approximately $W = 1$ m/s.

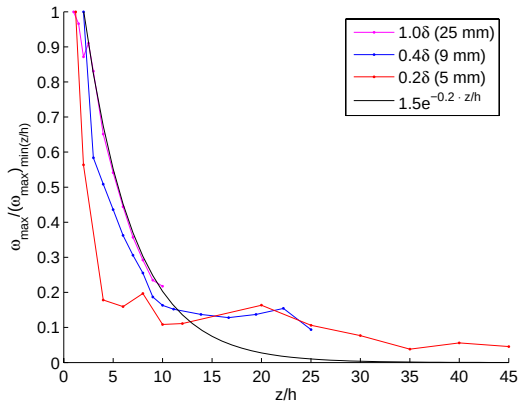

Figure 6. Maximum streamwise vorticity normalized by the maximum value in the most upstream plane for each respective case.

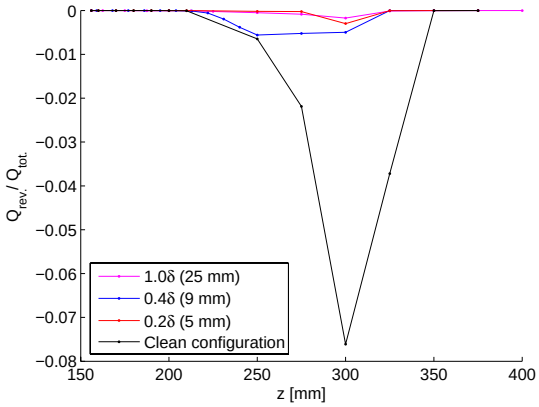

Figure 7. Reversed volumetric flow rate for every measurement position normalized by the total flow rate in each respective measurement plane.

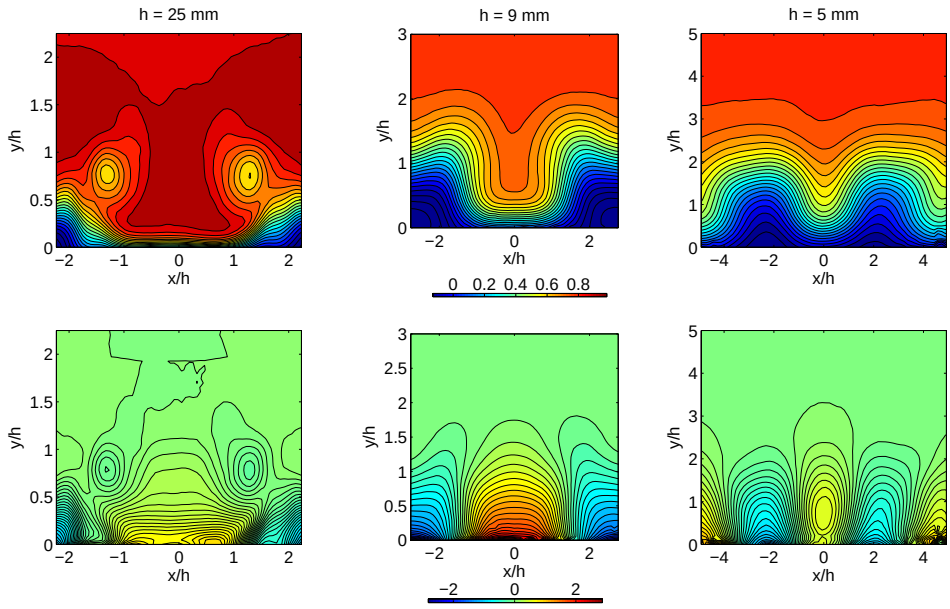

Figure 8. First row: Streamwise velocity component at $z = 250\ mm$ for the three VG cases. Second row: $(w(x,y) - \overline{w}(y))/\overline{w}(y)$, where $w(x,y)$ and $\overline{w}(y)$ denote the local value of the streamwise velocity component and the spanwise averaged value respectively.

To show the total effect over the entire span, a similar plot is made in figure 10, showing the spanwise averaged axial and normal velocity profiles. Also here it is seen for all streamwise positions that the separation has been suppressed by the VGs, as was also quantified in figure 7.

3.4. Comparison to computations

Figure 11 shows measured (left column) and computed (right column) velocity fields in the same fashion as in figure 5 for four downstream planes ($z_{VG}/h = 6$, 9, 13.9 and 22.2) for $h/\delta = 0.4$.

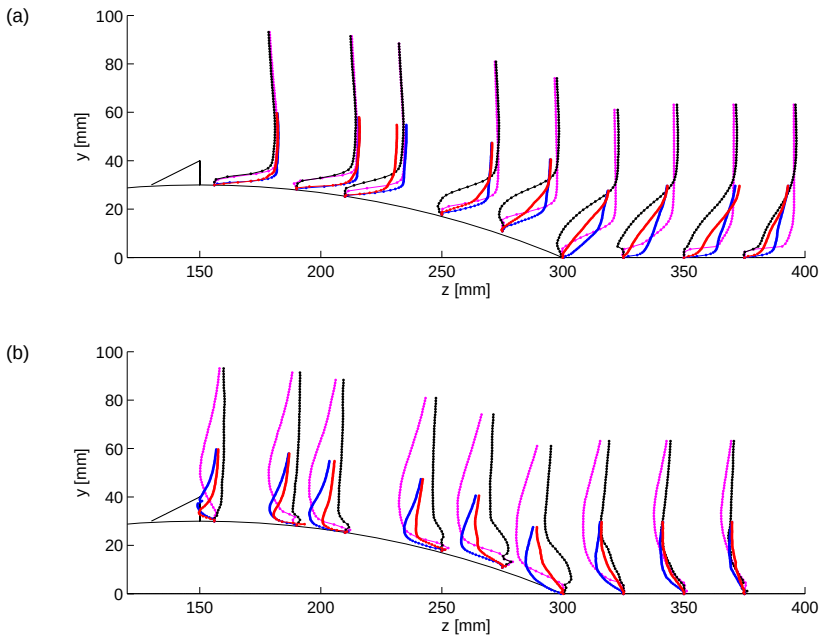

Figure 9. Streamwise (a) and normal (b) velocities in the downwash region ($x = 0$). The normal velocity has been scaled with a factor of four compared to the streamwise one. Black color corresponds to the clean configuration, magenta to 1δ, blue to 0.4δ and red to 0.2δ.

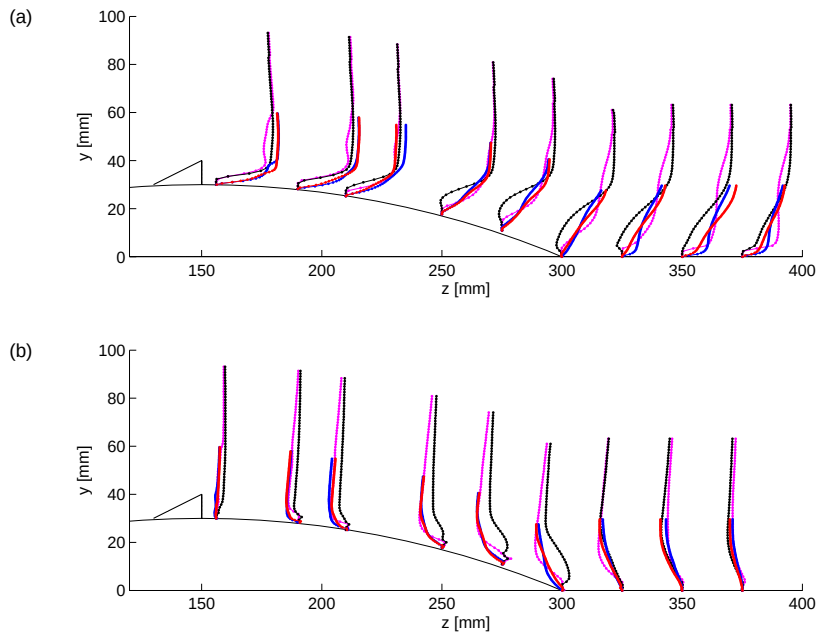

Figure 10. Streamwise (a) and normal (b) averaged axial velocity profiles. The normal velocity has been scaled with a factor of four compared to the streamwise one. Black color corresponds to the clean configuration, magenta to 1δ, blue to 0.4δ and red to 0.2δ.

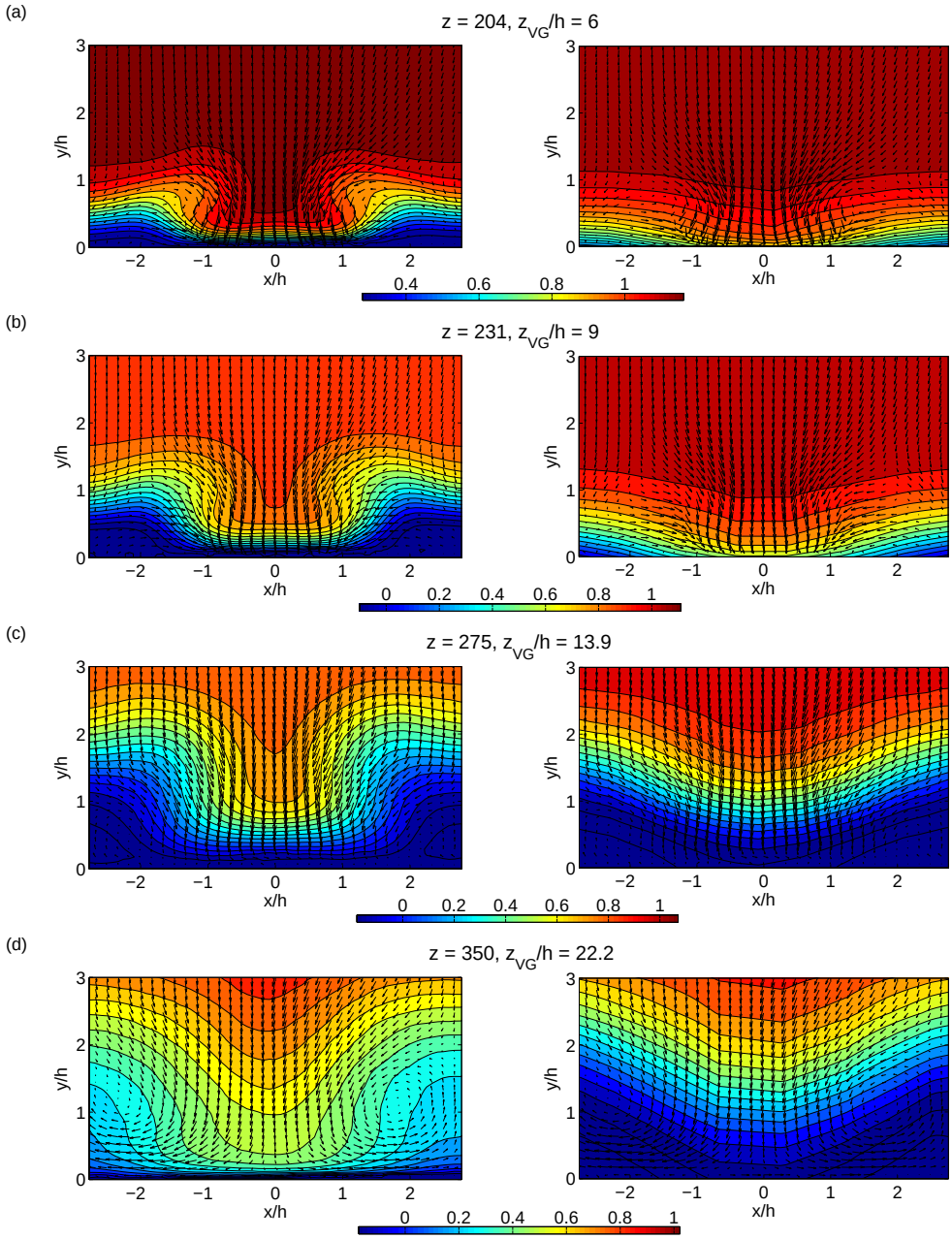

Figure 11. Velocity field plots of measurement data with in-plane components represented by vectors and the out-of-plane component represented by contours (left column) and corresponding computational data (right column) for four positions downstream of vortex generators ((a) $z_{VG}/h = 6$, (b) $z_{VG}/h = 9$, (c) $z_{VG}/h = 13.9$ and (d) $z_{VG}/h = 22.2$), case 0.4δ, showing the streamwise development of the flow field. The largest secondary velocities are of the order of 0.5 m/s, which can be compared to the free stream velocity of approximately $W = 1$ m/s.

The planes correspond to positions within and in the vicinity of the separation region in the clean configuration. The computations are not able to fully capture the primary and secondary velocities generated by the vortex generators and the effect of boundary layer thinning is not as evident as in the measurements.

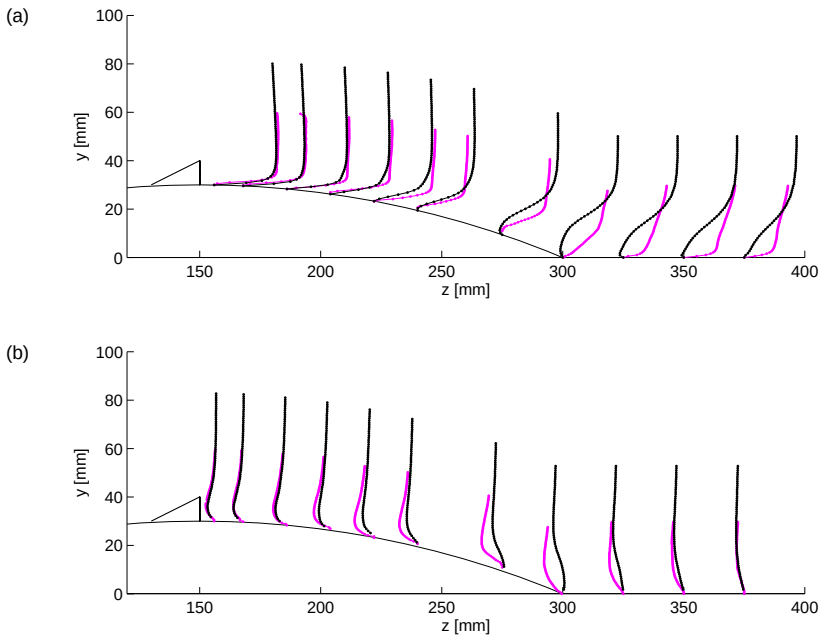

Figure 12. Streamwise (a) and normal (b) velocities for case 0.4δ in the downwash region ($x = 0$) for measured values (mangenta) and computations (black). The normal velocity has been scaled with a factor of two compared to the streamwise one.

Figure 12, showing the axial and normal velocity profiles in the symmetry plane ($x = 0$) for the measurements and the computations for the 0.4δ case, reveals difficulties for the computations to predict the flow within the separation region, which is expected for this turbulence model. The fact that the magnitude of the longitudinal velocity is underpredicted also stresses the fact that the turbulence model has difficulties predicting the large scale secondary velocity structures generated by the vortex generators.

4. Conclusions

It has been shown that it is possible to measure and resolve the flow created by a row of vortex generator pairs inducing counter-rotating vortices and their effect on the boundary layer using SPIV. It is apparent from the results that the vortex generators have the expected effect on the flow in the sense that they create large scale mixing near the wall. The measurements clearly show a structured vortex behind each vortex generator, whose development can be traced throughout the downstream planes. The devices have shown to be efficient more than 10 device heights downstream. The effect of the vortex generators on the amount of reversed flow is significant and shows a clear decrease in the amount of recirculation. In the future these measurements will be used to validate various numerical methods for calculating the flow behind vortex generators.

Comparison with the computational modeling of the vortex generators shows that the flow can be captured to some extent by steady-state RANS computations. However, they cannot accurately predict the flow in the separation region and there are difficulties modeling both the primary and secondary velocities. The convection of fluid transporting high momentum fluid from the outer flow into the near wall region is not well captured in the separation region.

Acknowledgments
The Danish Research Council, DSF, is acknowledged for their financial support of the project under Grant 2104-04-0020.

References

[1] Gad-el-Hak M and Bushnell D M 1991 *Journal of Fluids Engineering* **113** 5-30
[2] Taylor H D 1948 *United Aircraft Corp. Report No.* **M-15038-1**
[3] Lin J C 2002 *Progress in Aerospace Sciences* **38** 389-420
[4] Godard G and Stanislas M 2006 *Aerospace Science and Technology* **10** 181-191
[5] Wendt B J 2004 *AIAA Journal* **42** 2185-2195
[6] Mehta R D and Bradshaw P 1988 *Journal of Fluid Mechanics* **188** 529-546
[7] Angele K P and Grewe F 2007 *Journal of Fluids Engineering* **129** 226-235
[8] Øye S 1995 *9th IEA Symposium on Aerodynamics of Wind Turbines* ISSN 0590-8809, Stokholm, Sweden
[9] Schmidt J J 1997 *PhD thesis, DTU* **ET-PHD 97-01**